Advances in Aircraft and Spacecraft Science, *Vol. 8, No. 1 (2021) 31-51*
DOI: https://doi.org/10.12989/aas.2021.8.1.031

Temperature thread multiscale finite element simulation of selective laser melting for the evaluation of process

Kang-Hyun Lee[1a] and Gun Jin Yun*[2]

[1]Department of Mechanical & Aerospace Engineering, Seoul National University, Gwanak-gu Gwanak-ro 1 Seoul 08826, Republic of Korea
[2]Institute of Advanced Aerospace Technology, Seoul National University, Gwanak-gu Gwanak-ro 1, Seoul 08826, Republic of Korea

(Received August 28, 2020, Revised October 18, 2020, Accepted October 23, 2020)

Abstract. Selective laser melting (SLM), one of the most widely used powder bed fusion (PBF) additive manufacturing (AM) technology, enables the fabrication of customized metallic parts with complex geometry by layer-by-layer fashion. However, SLM inherently poses several problems such as the discontinuities in the molten track and the steep temperature gradient resulting in a high degree of residual stress. To avoid such defects, this study proposes a temperature thread multiscale model of SLM for the evaluation of the process at different scales. In microscale melt pool analysis, the laser beam parameters were evaluated based on the predicted melt pool morphology to check for lack-of-fusion or keyhole defects. The analysis results at microscale were then used to build an equivalent body heat flux model to obtain the residual stress distribution and the part distortions at the macroscale (part level). To identify the source of uneven heat dissipation, a liquid lifetime contour at macroscale was investigated. The predicted distortion was also experimentally validated showing a good agreement with the experimental measurement.

Keywords: selective laser melting; melt pool morphology; distortion; residual stress; finite element analysis; Ti-6Al-4V

1. Introduction

In the field of aerospace, many kinds of alloys including aluminum alloys (Çam and Koçak 1998, Han *et al.* 2017, Kaci *et al.* 2017) and Ti-6Al-4V (Boyer 1996, Singh *et al.* 2017) which is an $\alpha + \beta$ titanium alloy are in high demand due to their low density and the high specific strength. However, the traditional manufacturing processes for these alloys such as molding, forging and casting result in an expensive manufacturing cost, long production time, and a large waste of material. Compared to the traditional methods, the additive manufacturing (AM) process enables the fabrication of products with complex shapes from computer-aided design (CAD) models. Among the AM processes, selective laser melting (SLM) is one of the most widely used powder bed-based processes that utilizes a high-intensity laser beam to selectively fuse the metallic powder to create a 3-dimensional object (Gu *et al.* 2012, Yap *et al.* 2015). During an SLM

*Corresponding author, Professor, E-mail: gunjin.yun@snu.ac.kr
[a]Ph.D. Student, E-mail: kyu5923@snu.ac.kr

Copyright © 2021 Techno-Press, Ltd.
http://www.techno-press.org/?journal=aas&subpage=7 ISSN: 2287-528X (Print), 2287-5271 (Online)

process, a roller or a recoater blade deposits a thin layer of powder from the reservoir onto the build plate or previously solidified layers. Then, the laser beam selective fuses the powder particles following the predefined scanning paths. After scanning one layer, the process of powder deposition and laser scanning is repeated until the part is built completely. As the bulk solid part is built in a layer-by-layer fashion, the SLM process enables the fabrication of metallic parts with complex geometries and added functionalities (Herzog *et al.* 2016).

Although the SLM process provides a great advantage in manufacturing, the SLM printed parts suffer from various manufacturing defects. Since the laser beam energy is highly concentrated in the spot diameter ranges from 30 to 100 μm (Shi *et al.* 2018) with the scanning speed of hundredths of millimeters per second (Dilip *et al.* 2017), rapid consolidation up to 10^{6-8} K/s occur due to the short time of interaction (Gu *et al.* 2014, Das *et al.* 2010). The generated high temperature gradient inevitably leads to an inhomogeneous thermal distribution which eventually results in the formation of residual stresses and the part distortions (Buchbinder *et al.* 2014, Mercelis and Kruth 2006). The porosity is also a major defect in the SLM process which is often associated with the lack-of-fusion (Bruna-Rosso *et al.* 2018) or the keyhole mode melting (Shrestha *et al.* 2019). Furthermore, many transient physical phenomena including the melting and the partial vaporization of the material (Verhaeghe *et al.* 2009), and the melt pool dynamics (Zhao *et al.* 2017) complicate the understanding of the SLM process.

In order to understand and optimize the SLM process, numerical models in various scales have been developed and utilized in recent years. Since the analyses of the SLM process at different scales provide different results, their roles are also different for the understanding of the process. For instance, the microscale melt pool analysis is used to obtain the temperature history modeling the exact laser scanning with the moving heat flux. Hence, the laser beam process parameters including the laser power, the scanning speed, and the layer thickness are accounted for based on the real printing process. It is also worth noting that as the part qualities including the dimensional accuracy, the mechanical properties, and the surface roughness are affected by the formation of solidified tracks (Yadroitsev *et al.* 2010), the most well-known approach for optimizing the SLM process is the investigation of the single-track formation with melt pool evolution (Roy *et al.* 2018, Zhang *et al.* 2019, Lee and Yun 2020a). Roy *et al.* (2018) proposed a thermal analysis model considering the consolidation effect based on the thermodynamically-consistent phase field-approach (Wang *et al.* 1993). The authors found that the incorporation of the consolidation effect reduces the laser power absorption and leads to more accurate predictions of the melt pool dimensions with given process parameters. Zhang *et al.* (2019) developed a heat transfer finite element model with anisotropically enhanced thermal conductivity and varied absorptivity. They proposed approximate functions of the process parameters for the calibrated properties and achieved a mean error of 7.3% for the prediction of melt pool depth. Lee *et al.* (Lee and Yun 2020a) proposed a hybrid heat source model for melt pool analysis to incorporate the transition of the melting mode. The proposed model takes into account the different optical thickness for the porous and dense material to predict the melt pool evolution under both the conduction mode and the keyhole mode. Their results also showed that the commonly used surface Gaussian heat flux model could be inappropriate for the SLM process simulation due to the existence of powder material.

For evaluation of the residual stress and the distortion considering the geometrical effect of the part, a macroscale analysis needs to be conducted. However, modeling of every single track during the multi-layer SLM process is not feasible since it takes several hours (Ansari *et al.* 2019) for a single layer analysis even with a powerful work station. Thus, it is important to build an efficient

model to obtain accurate prediction results with reasonable computational efficiency at macroscale. Chen *et al.* (2019a) proposed a multiscale simulation framework for efficient prediction of the residual stress and distortion of SLM printed parts using an inherent strain model (Liang *et al.* 2018). In the proposed framework, a calibrated microscale simulation considering the exact scanning paths is conducted first and the obtained anisotropic inherent strains are applied to the quasi-static equilibrium finite element model at part scale. Furthermore, several physical layers are considered as one numerical layer at part scale and are activated in layerwise fashion. Similar to this method, Li *et al.* (2017) divided the macroscale part model into several mesoscale layers to reduce the computation cost. The authors also developed a temperature thread multiscale model of the SLM process with an equivalent body heat flux based on the microscale melt pool analysis results. Since the heating and the cooling processes are modeled using the equivalent body heat flux at macroscale, the phase transition with several re-melting processes is incorporated in their model.

In this study, a temperature thread multiscale simulation framework for the SLM process is introduced to evaluate the SLM process. An enhanced microscale melt pool analysis model is used to predict the temperature history considering the increase of absorptivity and the enhanced conductivity which are dependent on the melt pool morphology. The evaluation of the laser process parameters for the formation of a stable molten track is conducted at this scale considering the melt pool size and the material state in the scanned track. Then, the equivalent body heat flux is modeled based on the results from the microscale analysis and is applied to the mesoscale hatch layers in the part model. At this scale, the residual stress is obtained as well as the part distortions, and the results are discussed with the heat dissipation history in the part. The experimental validation for the prediction of part distortion is also presented with the fabrication of cantilever using a commercial laser powder bed fusion (L-PBF) machine.

2. Simulation methodology

A typical schematic diagram of the SLM process with the related thermal boundary conditions is as shown in Fig. 1. During the SLM process, a laser beam moves following the predefined scanning paths on the powder bed with the layer thickness d_p. The laser energy is highly concentrated in the beam spot size and the energy is enough to melt the material which leads to the formation of a melt pool (Fu and Guo 2014). Then, the molten material is consolidated rapidly as the center of the laser beam moves away from the previous position forming a bulk solid as depicted in Fig. 2. After scanning the whole single layer, the powder material is deposited again and scanned with the pre-defined scanning paths according to the 3-dimensional CAD data. This process is repeated until the scan of the last layer is finished.

In order to investigate and evaluate the SLM process at different scales, a multi-scale analysis framework was used in this study as shown in Fig. 3. The idea of bridging the melt pool scale analysis to part scale analysis of the SLM process was originally presented by (Li *et al.* 2017). First, the microscale melt pool analysis was conducted to obtain the temperature history and the melt pool morphology considering the moving laser beam heat source. Secondly, the equivalent body heat flux model at mesoscale was defined using the obtained temperature history from the microscale melt pool analysis. The equivalent body heat flux was then applied in the sliced mesoscale hatch layers to obtain the residual stress distribution and deformation of the part at the macroscale.

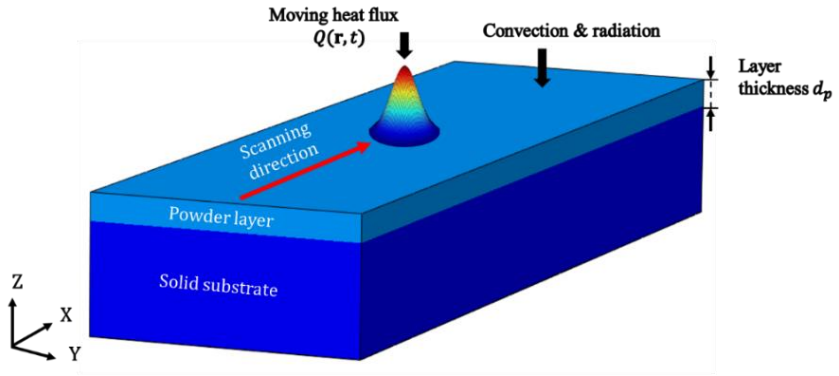

Fig. 1 Schematic diagram of SLM process with related thermal boundary conditions

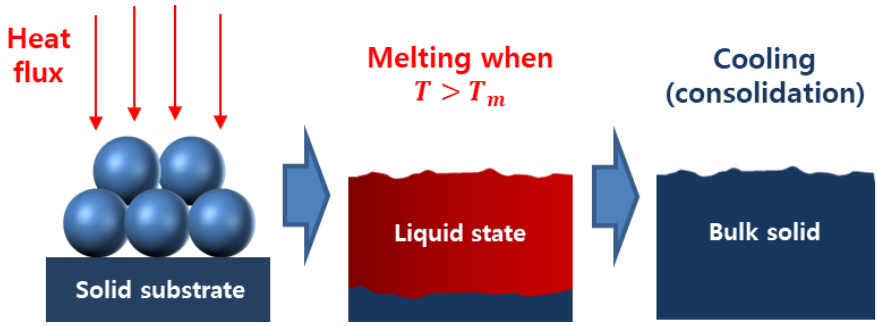

Fig. 2 Melting and consolidation of powder material during SLM process

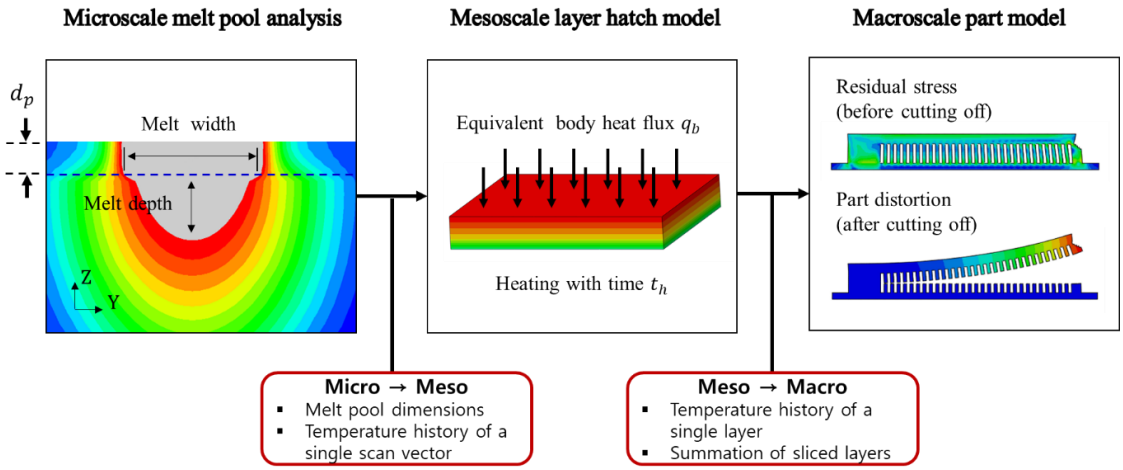

Fig. 3 Multi-scale analysis framework of SLM process

2.1 Thermo-mechanical material behavior

To analyze the SLM process with reasonable accuracy, the material behavior needs to be modeled considering the important physical phenomena including the phase transition

Table 1 Thermal material properties for Ti-6Al-4V (Verhaeghe *et al.* 2009, Boivineau *et al.* 2006, Seifter *et al.* 1998, Mills 2002, Fan and Liou 2012, Welsch *et al.* 1993)

Property	Symbol	Value
Conductivity for porous state [W/mm K]	k_p	0.3×10^{-3}
Conductivity for dense state [W/mm K]	k_d	26.0×10^{-3}
Volumetric heat capacity for solid state [J/mm^{3}K]	C_s	3.65×10^{-3}
Volumetric heat capacity for liquid state [J/mm^{3}K]	C_l	4.98×10^{-3}
Latent heat of fusion [J/mm^3]	L_f	1.26
Solidus temperature [K]	T_s	1878
Liquidus temperature (solid - liquid) [K]	T_l	1923
Latent heat of vaporization [J/mm^3]	L_v	44.3
Liquidus temperature (liquid - vapor) [K]	T_{vl}	3563
Vaporized temperature [K]	T_{vp}	3663

(melting/vaporization/consolidation) with severe temperature fluctuation. The temperature-dependent thermo-mechanical material properties also vary drastically with one or more heating and cooling cycles. Furthermore, the material states including the powder state which is the initial state for the deposited material on the substrate, the liquid state when the temperature exceeds the liquidus temperature T_l, the vaporized state when the temperature exceeds the vaporized temperature T_{vp}, and the bulk solid state for the consolidated material after cooling need to be distinguished at every time increment during the analysis. The proposed simulation framework for the sequentially coupled thermomechanical analysis was built using the commercial finite element software ABAQUS/Standard. For both of the thermal and the mechanical analysis, 1st order 3-dimensional 8 node linaer hexahedron elements (DC3D8, and C3D8) were used.

2.1.1 Thermo modeling

During the SLM process, the material undergoes the phase transition from solid to liquid due to the absorption of the laser beam energy. If the initially porous material(powder) turns into a dense liquid state, the material becomes a dense solid state after sufficient cooling. In order to incorporate this material state change mechanism, Roy *et al.* (Roy *et al.* 2018) presented a thermal energy balance equation based on the thermodynamically-consistent phase-field approach (Wang *et al.* 1993). They used two state variables to track the material state considering the melting and the degree of consolidation. To consider the latent heat of vaporization in the energy balance equation, the vaporization term also needs to be added with the corresponding state variable as follows

$$\frac{de}{dt} - \nabla \cdot k\nabla T - Q(\mathbf{r}, t) = 0 \tag{1}$$

$$e = C_s(\psi)T + p(\phi_m)\{L_f + [C_l - C_s(\psi)](T - T_m)\} + L_v p(\phi_v) \tag{2}$$

Eq. (1) is the thermal energy balance equation where e is the energy density, t is the time, k is the thermal conductivity, T is the temperature, $\mathbf{r}$ is the coordinate vector, and Q is the applied heat flux. Eq. (2) is the energy density where C_s is the volumetric heat capacity for solid

Table 2 Temperature-dependent elastic modulus, thermal expansion coefficient, yield stress of Ti-6Al-4V (Rangaswamy *et al.* 1999)

Temperature [K]	Elastic modulus, E [GPa]	Thermal expansion coefficient, α $[10^{-6}/\mathrm{K}]$	Yield stress, σ_{y0} [GPa]
296	125	8.78	1000
533	110	9.83	630
589	100	10.14	630
700	100	10.71	525
755	80	10.97	500
811	74	11.22	446
923	55	11.68	300
1073	27	12.21	45
1098	20	12.29	25
1123	5	12.37	5
1923	0.1	12.5	0.1

Table 3 Temperature-dependent Poisson ratio and plastic modulus of Ti-6Al-4V (Roberts 2012, Fukuhara and Sanpei 1993, Vanderhasten *et al.* 2008)

Temperature [K]	Poisson ratio	Temperature [K]	Plastic tangent modulus, E_p [GPa]
301	0.34	298	2.87
380	0.35	573	2.88
479	0.35	773	1.62
579	0.36	873	0.41
675	0.36	923	0.40
802	0.37	973	0.15
881	0.38	1023	0.01
979	0.38	1073	0.03
1068	0.39	1123	0.05
1233	0.42	1173	0.05
1275	0.45	1223	0.03
1307	0.44	1248	0.02
1319	0.43	1323	0.02

state material, C_l is the volumetric heat capacity for liquid state material, p is the interpolation function for the phase transition, ψ is the consolidation parameter, ϕ_m is the phase parameter for melting, ϕ_v is the phase parameter for vaporization, T_m is the average melting temperature, L_f and L_v are the latent heat of fusion and the latent heat of vaporization respectively. The thermal material properties of Ti-6Al-4V are as listed in Table 1 from several references. The detailed formulation for the thermal problem of the SLM process can be found in our previous work (Lee and Yun 2020b).

2.1.2 Mechanical model

For the sequentially coupled thermo-mechanical analysis of the SLM process, the temperature and the material state obtained from the thermal analysis are used as input parameters in the subsequent mechanical analysis. The total strain increment $\mathrm{d}\boldsymbol{\varepsilon}^{\mathrm{T}}$ including the elastic strain $\mathrm{d}\boldsymbol{\varepsilon}^{\mathrm{e}}$, the plastic strain $\mathrm{d}\boldsymbol{\varepsilon}^{\mathrm{p}}$, and the thermal strain $\mathrm{d}\boldsymbol{\varepsilon}^{\mathrm{th}}$ can be expressed as follows

$$\mathrm{d}\boldsymbol{\varepsilon}^{\mathrm{T}} = \mathrm{d}\boldsymbol{\varepsilon}^{\mathrm{e}} + \mathrm{d}\boldsymbol{\varepsilon}^{\mathrm{p}} + \mathrm{d}\boldsymbol{\varepsilon}^{\mathrm{th}} \tag{3}$$

$$\mathrm{d}\boldsymbol{\varepsilon}^{\mathrm{th}} = \alpha \Delta T \tag{4}$$

where α is the thermal expansion coefficient. For plasticity, the simple isotropic hardening model which is also commonly adopted in the stress analysis of the SLM process (Vastola *et al.* 2016, Roberts 2012, Chen *et al.* 2019b) was used with von Mises yield function as follows

$$\boldsymbol{\sigma} = \mathbf{D}\boldsymbol{\varepsilon}^{\mathrm{e}} \tag{5}$$

$$f = \sigma_e - r - \sigma_{y0} \tag{6}$$

$$\sigma_e = \left(\frac{3}{2}\boldsymbol{\sigma}' : \boldsymbol{\sigma}'\right)^{1/2} \tag{7}$$

$$d\boldsymbol{\varepsilon}_{\mathbf{p}} = d\lambda \frac{\partial f}{\partial \boldsymbol{\sigma}} \tag{8}$$

where $\boldsymbol{\sigma}$ is the stress tensor, $\mathbf{D}$ is the material stiffness matrix, f is the yield function, σ_e is the equivalent stress which is also known as von Mises stress, r is the hardening stress, σ_{y0} is the initial yield stress, and $d\lambda$ is the plastic multiplier. The temperature-dependent mechanical properties of Ti-6Al-4V from several references are as shown in Tables 2 and 3.

2.2 Microscale melt pool analysis

During the SLM process, the interaction between the laser and the material for process involves various physical phenomena including the volume shrinkage of the powder bed, material vaporization, multiple reflections of the laser beam, and fluid dynamics such as Marangoni convection (Verhaeghe *et al.* 2009, Zhao *et al.* 2017, Leung *et al.* 2018). In order to achieve improved prediction of the melt pool morphology, these physical mechanisms should be incorporated in the numerical model.

To incorporate the typical mechanisms of the SLM process in a numerical simulation, a melt pool analysis model considering the different melting modes (conduction/keyhole) and the different absorption mechanisms of porous/dense material (Lee and Yun 2020a) was used in this study. The proposed model considers the volume shrinkage of the powder bed by deactivating the partial volume of the powder layer (which is assumed to be 0.4 (Hussein *et al.* 2013) in this study) when it becomes the liquid state. The vaporized material is also deactivated and the surface where the laser interacts is captured at every time increment to define the moving heat flux. Furthermore, the model considers the effective absorptivity which is dependent on the morphology of the melt pool to incorporate the keyhole mode melting based on the experimental measurement for 316L stainless steel (Trapp *et al.* 2017). In this study, a melt pool aspect ratio dependent absorptivity

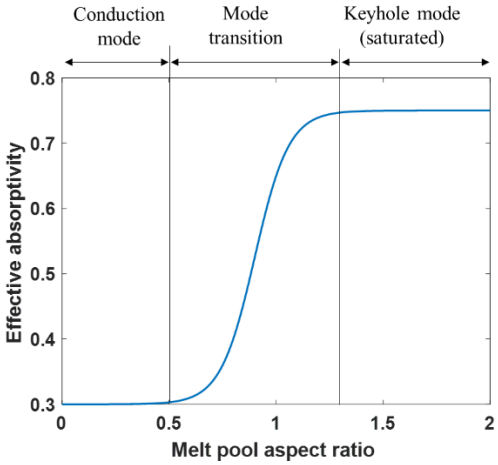

Fig. 4 Effective absorptivity dependent on melt pool morphology

(Section 2.2.1) was used since there is no reliable experimental data for varying effective absorptivity of Ti-6Al-4V. To apply the melt pool morphology dependent effective absorptivity, the melt pool dimensions were computed at every time increment. The model also utilizes the calibrated anisotropic enhanced thermal conductivity which is dependent on the melt pool depth to account for the effect of Marangoni and buoyancy-driven convection. The detailed modeling procedure for computing the melt pool dimensions at every time increment during the analysis is introduced in our previous work (Lee and Yun 2020a).

2.2.1 Effective absorptivity of dense material

Trapp *et al.* (Trapp *et al.* 2017) found out that the effective absorptivity sharply increases at a critical keyhole mode threshold and the saturated value is more than twice the absorption coefficient for the conduction mode regime. Moreover, Queva *et al.* (2020) pointed out that the relevant value for the keyhole mode melting would be between 0.65 and 0.75 which is higher than the simple approximation for absorptivity value which is $A = 1 - R$, where R is the reflectivity. Zhao *et al.* (2017) also found that the melt pool aspect ratio(γ =depth/width) is close to 0.5 which is an indication of conduction mode melting, and the value rapidly increases to 1.3 and remains unchanged indicating the saturated keyhole mode melting. Thus, a simplified assumption for effective absorptivity with varying melt pool morphology is proposed in this study as shown in Fig. 4. When the melt pool aspect ratio is less than 0.5, which leads to a bowl-shaped melt pool, the melting mode is assumed to be the conduction mode regime (Dilip *et al.* 2017). In this region, the effective absorptivity of Ti-6Al-4V is assumed to be $A_{min} = 0.3$ (Queva *et al.* 2020, Dausinger and Shen 1993). When the aspect ratio reaches 0.5, the absorptivity starts to increase up to 0.75 since the saturated value of absorptivity is about 0.7-0.8 (Trapp *et al.* 2017, Fabbro 2010, Del Bello *et al.* 1991). An equation for the smooth transition of the melting mode was utilized in this study as follows

$$A(\gamma) = \left(\frac{A_{max} - A_{min}}{2}\right)\left\{\tanh\left[\frac{\alpha\left(\gamma - \frac{\gamma_1 + \gamma_2}{2}\right)}{\gamma_2 - \gamma_1}\right] + 1\right\} + A_{min} \tag{9}$$

where $A_{max} = 0.75$ is the saturated value, $\gamma_1 = 0.5$ is the point at which the absorptivity starts to increase, $\gamma_2 = 1.3$ is the point at which the absorptivity saturates, and α is the parameter for the smooth transition which was assumed to be 5.0 in this study.

2.2.2 Enhanced conductivity

In order to effectively incorporate the contribution of the melt pool convection in the model, the anisotropically enhanced conductivity has been commonly used to improve the accuracy of the melt pool prediction (Zhang *et al.* 2019, Kamara *et al.* 2011, Liu *et al.* 2018). The anisotropically enhanced conductivity for the liquid state material can be expressed as follows

$$k_x = \lambda_x k, \qquad k_y = \lambda_y k, \qquad k_z = \lambda_z k \tag{10}$$

where λ_x, λ_y and λ_z are the anisotropically enhanced factors of thermal conductivity, which are set to 1 when the temperature is below the melting temperature. The enhanced factors can be either constant (Kamara *et al.* 2011, Liu *et al.* 2018) or functions (Zhang *et al.* 2019, Lee and Yun 2020a). In this paper, the melt pool geometry-dependent enhanced factors were used with the melt pool aspect ratio γ as follows

$$\lambda_z = p_1\gamma + p_2, \qquad \lambda_x = \lambda_y = p_2 \tag{11}$$

where p_1 and p_2 are the fitting parameters. The value of p_2 was assumed to be 2.5 (Lampa *et al.* 1997) and the value of p_1 was calibrated for the improved prediction of the melt pool depth using the existing experimental result as shown in the next section.

2.2.3 Simulation model and calibration

The model symmetric about the $x - z$ plane with the thermal boundary conditions is as shown in Fig. 5. The moving heat flux was applied along the central line towards the direction x. The convection and radiation boundary conditions were applied with the ambient temperature equals to room temperature. The biased mesh scheme was used in the model where the finer mesh size is assigned at the top powder bed with a mesh size of $10 \times 10 \times 6$ μm.

In order to calibrate the fitting parameter p_1 in the Eq. (11), the experimental results in the existing research study (Dilip *et al.* 2017) were used. Figs. 6 and 7 show the comparisons between the predicted melt pool dimensions and the experimental results. The simulation was conducted with $p_1 = 20$, which was chosen by trials and errors, and the melt pool dimensions were evaluated at the stable state after the heat source passes the center of the scanning path. It is shown that as the laser power increases and the scanning speed decreases, the size of the melt pool increases due to the higher volumetric energy density(VED) (Ciurana *et al.* 2013). The results show that the predicted values are in good agreement with the experiment with the mean errors of the predictions 10.59% and 3.28% for the melt pool depth and the width respectively.

2.3 Equivalent body heat flux at mesoscale

Using the obtained temperature history and the melt pool dimensions in the microscale melt pool analysis, an equivalent body heat flux q_b can be developed as follows to obtain similar thermal cycles at a larger scale of the analysis (Li *et al.* 2017)

$$q_b = \frac{AP}{d_s d_m H} \tag{12}$$

where A is the effective absorptivity, P is the laser power, d_s is the laser spot diameter, d_m is the melt pool depth, and H is the hatch distance. However, since the absorptivity varies with the melting mode as explained in Section 2.2.1, the modified form of Eq. (12) is proposed as follows

$$q_b = \frac{A(\gamma_s)P}{d_s d_m H} \tag{13}$$

where γ_s is the aspect ratio of the predicted melt pool morphology at a stable state, P is the laser power, d_s is the laser spot diameter, d_m is the melt pool depth, H is the hatch distance, and $A(\gamma_S)$ is the effective absorptivity in Eq. (9). The body heat flux was applied to the mesoscale hatched layer with the exposure time of heating time t_h obtained in the melt pool analysis as explained in Section 3.2.

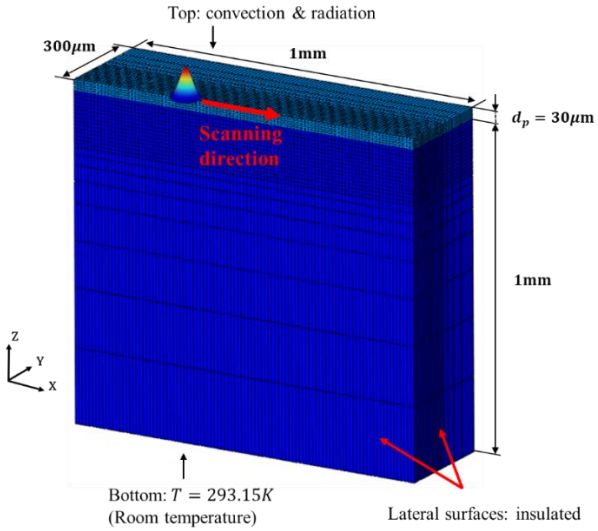

Fig. 5 Schematic of simulation for melt pool analysis

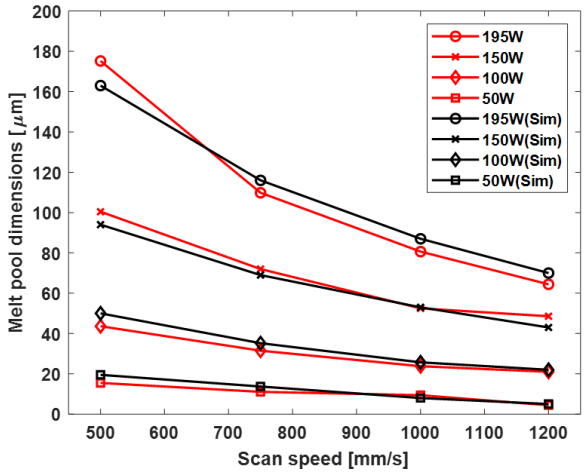

Fig. 6 Predicted melt pool depth with the experimental results

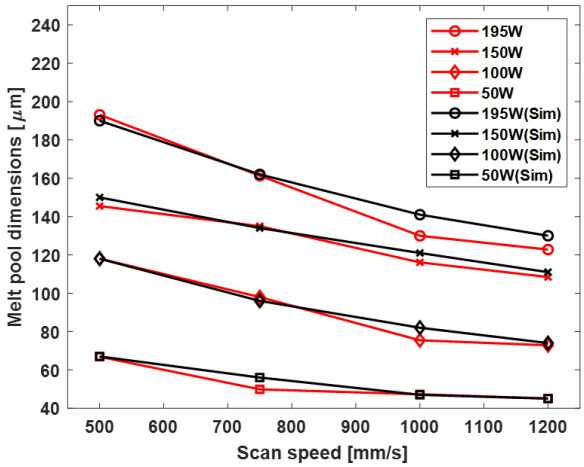

Fig. 7 Predicted melt pool width with the experimental results

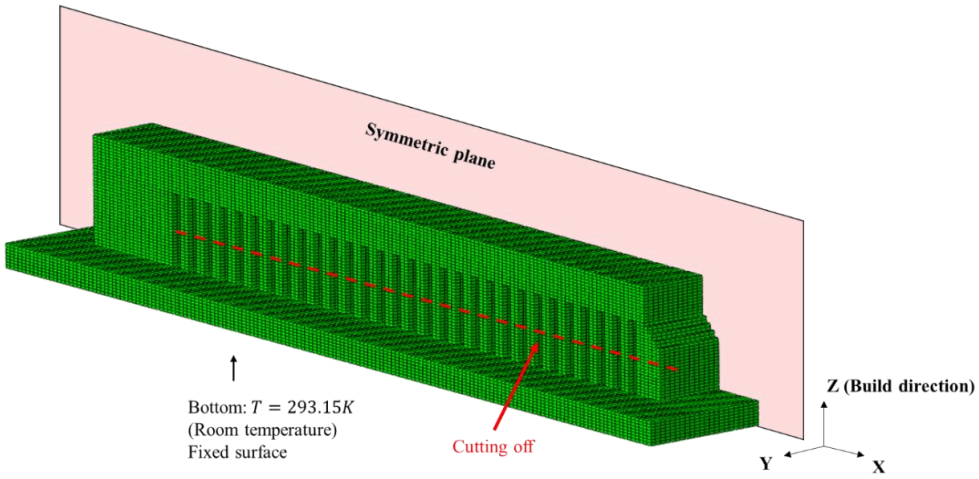

Fig. 8 Macroscale part model of cantilever with support

Table 4 Part dimensions (full model) for cantilever

Dimension	Value
Length [mm]	72
Width [mm]	12
Height [mm]	9
Cut-off height [mm]	2.9

2.4 Macroscale part model

For the macroscale analysis of the SLM process, a half symmetric model of a cantilever with support was modeled as shown in Fig. 8. The dimension of the original full model is as shown in Table 4. To aid the convergence of the problem and the slicing of the layers, layerwise Cartesian

mesh was generated for the whole model with a uniform element size of $500 \times 500 \times 250$ μm.

The additive mechanism for the multi-layer process was modeled using the element activation/deactivation method. First, the whole part including the support structure was divided into 9 mesoscale hatch layers with a height of 1 mm. When the first layer was in process, which means that the layer was heated up by the equivalent body heat flux, the other layers were not activated. After the process for the first layer was finished, the second layer was activated and the equivalent body heat flux is now applied to the newly added layer. This process was repeated until the process of the last layer was completed with the cooling time of 100 seconds. After the whole additive process ended and the temperature cooled down to room temperature, the support was cut for the evaluation of the part distortion due to the residual stress. In the simulation, the cutting of the support was modeled by deactivating the element along with the cut-off line (Fig. 8).

3. Results and discussion

In this section, the obtained analysis results from each scale are discussed in detail. First, the results from the microscale melt pool analysis are investigated to evaluate the laser beam process parameters. The predicted residual stress distribution and the part distortion at macroscale are also evaluated with experimental validation. For experimental validation, the cantilever beam (Fig. 8) with the given dimensions (Table 4) was fabricated using an EOS M290 L-PBF machine. The process parameters used for the analysis and the fabrication of the specimen are as listed in Table 5. Those are the recommended parameters by EOS for the SLM process of Ti-6Al-4V.

Table 5 SLM process parameters for analysis

Parameter	Value
Laser power [W]	280
Scanning speed [mm/s]	1200
Hatch distance [μm]	140
Layer thickness [μm]	30

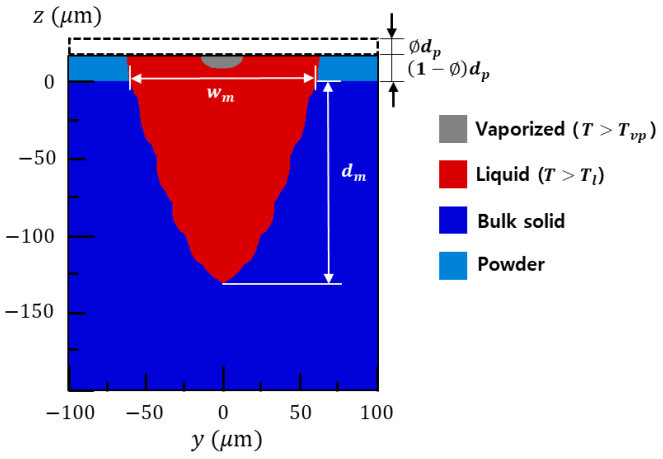

Fig. 9 Cross-section image of melt pool from single-track melt pool analysis

3.1 Melt pool morphology

The predicted melt pool morphology using the proposed microscale model (Section 2.2) is as shown in Fig. 9. The red color denotes the molten region with the width w_m of 152 μm and the depth d_m of 131 μm. In particular, the melt pool morphology is an important indicator to achieve enough bonding of the scanned track to the substrate or former processed layer. Since the hatch distance H was 140 μm and the layer thickness d_p was 30 μm, it is evident that the enough melt pool size was achieved to completely wet the scanned track. Thus, it is unlikely that the problem of the lack-of-fusion porosity (Bruna-Rosso *et al.* 2018) arises with the given process parameters. Furthermore, there was partial vaporization of the material observed in the track with the given process condition with the melt pool aspect ratio of 0.86 which indicates the evolution of keyhole (not saturated). The advantage of using the melt pool morphology dependent properties considering the different absorption mechanisms of porous and dense material is that the model can approximate the degree of vaporization ($\eta =$ vaporized volume/molten volume) considering the keyhole mode melting (Lee and Yun 2020a). Since only the vaporization of the partial volume of powder material with $\eta = 0.015$ was observed compared to the intense keyhole mode melting ($\eta = 0.04\sim$) (Lee and Yun 2020a), it could be said that the process with the given parameters is less likely to involve severe keyhole mode defects (Shrestha *et al.* 2019).

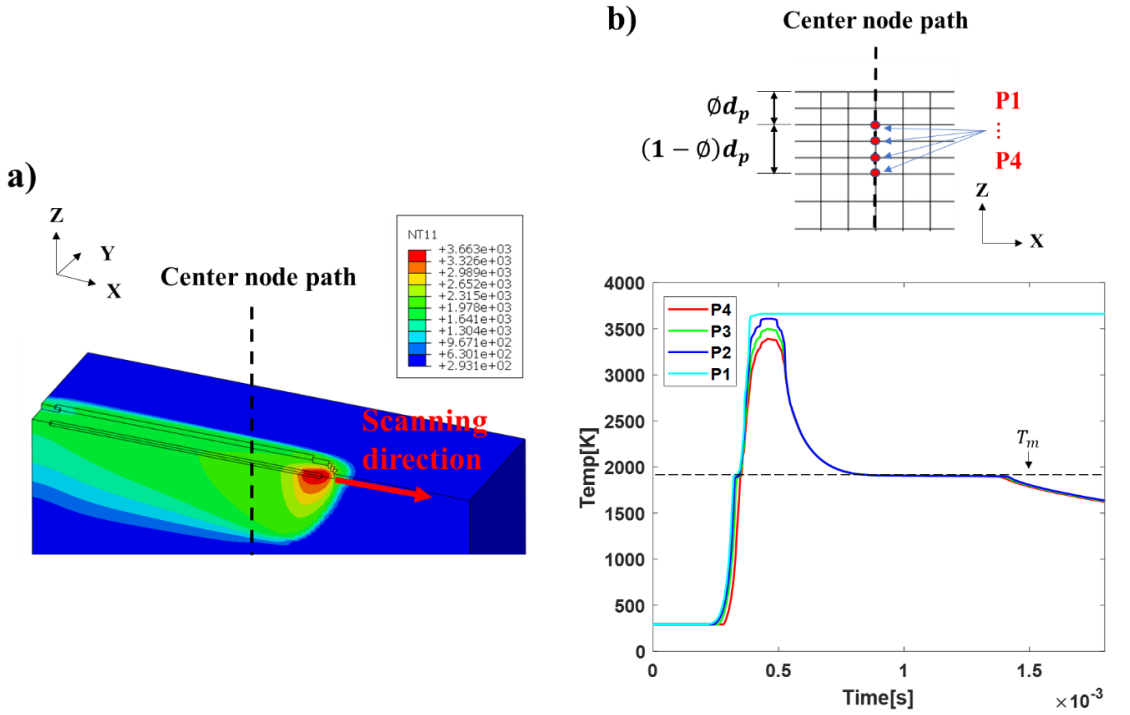

(a) Temperature distribution

(b) Nodal temperature at each nodal point on the center node path

Fig. 10 Temperature history with moving heat flux (a) temperature distribution and (b) nodal temperature at each nodal point on the center node path

3.2 Temperature history

The transient temperature distribution contour with the moving heat flux is as shown in Fig. 10(a). As shown in the contour with only activated elements, a steep temperature gradient was generated in the vicinity of the moving heat flux. In order to evaluate the transient temperature evolution during the single track scanning, the nodal points of the powder layer on the central line parallel to the z-axis were chosen as shown in Fig. 10(b). Since the partial volume of the powder layer shrinks due to the initial powder porosity ($\emptyset = 0.4$), the temperature histories of 4 nodal points (P1-P4) were investigated. As shown in the transient temperature histories shown in the graph (Fig. 10(b)), the temperature rapidly increased as the center of the moving heat flux approaches the middle of the scanning track. As the center of the moving heat flux moves away from the point, the temperature then decreased due to the conduction to the surrounding material, the heat convection, and the radiation with the release of the latent heat of fusion. In particular, the nodal temperature of P1 remained at the vaporized temperature (3663K) since the corresponding element was deactivated after vaporization as shown in Fig. 10a. The average heating time t_h for reaching the maximum temperature from the room temperature 293.15K was about 0.2 milliseconds which was used as an exposure time for the equivalent body heat flux (Eq. (13)).

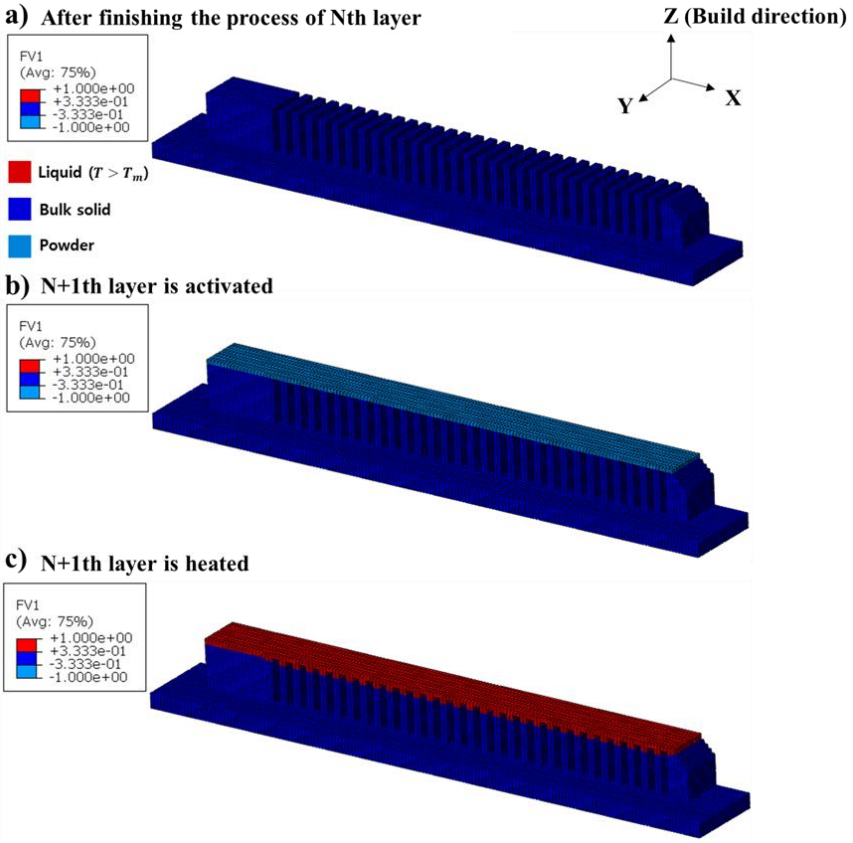

Fig. 11 Material state variation with element activation for simulation of the multi-layer SLM process

3.3 Phase transition

The material state evolution with the element activation process is as shown in Fig. 11. When a new layer was activated, the material states for the elements in the activated layer were defined as powder state as shown in Fig. 11(b). Then, the material was heated up by the equivalent heat flux and the material states for the elements in the activated layer turned into the liquid state as shown in Fig. 11(c). The material states of some elements in the previous layer also became liquid state since the heat flux was high enough to re-melt the solidified material. The additional field variable (FV1) was used to track the material state during the simulation (1: liquid, 0: bulk solid, 3: powder).

3.4 Residual stress

Due to the formation of the high temperature gradient and the non-uniform thermal and plastic strain, the high degree of residual stress can remain in the part after the process ends (Kruth *et al.* 2004). The predicted residual stress distributions before and after cutting off the support are depicted in Fig. 12. The maximum von Mises stress was about 1166 MPa before the cut-off and decreased to 1060MPa after cut-off which are both higher than the yield stress of Ti-6Al-4V (1000MPa) at room temperature. This means that the plastic deformation took place with hardening after the process was finished. In particular, the stress in the length direction (S11) was concentrated in the upper region of the cantilever as shown in Fig. 12(a). After cutting off the support (Fig. 12(b)), the accumulated residual stress was released with the part distortion.

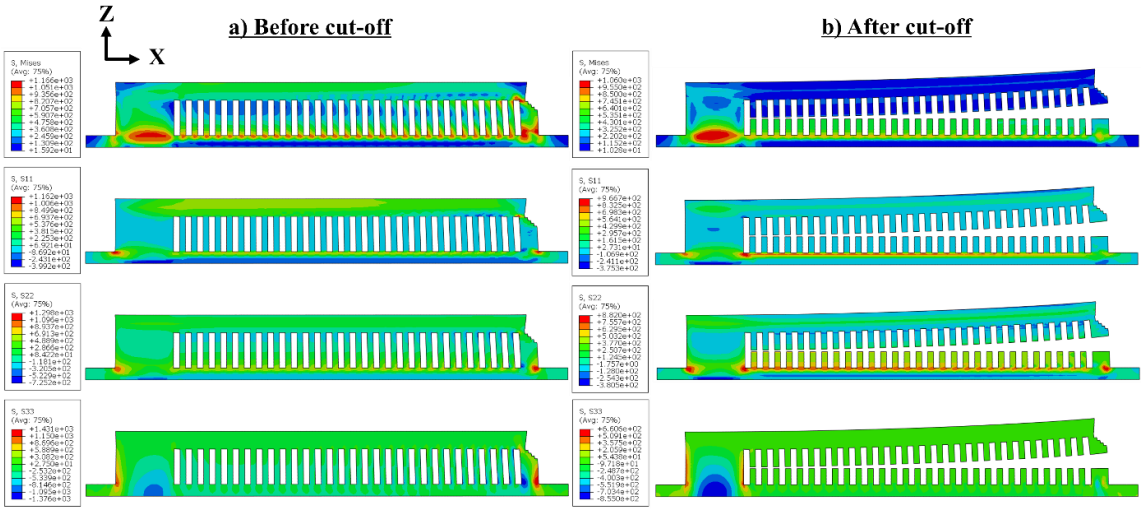

Fig. 12 Residual stress distribution of the part model (a) before cut-off and (b) after cut-off

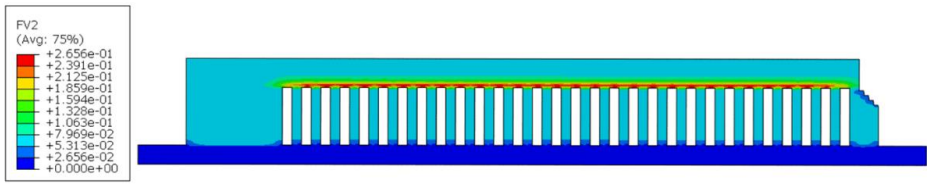

Fig. 13 Liquid lifetime contour of the part model

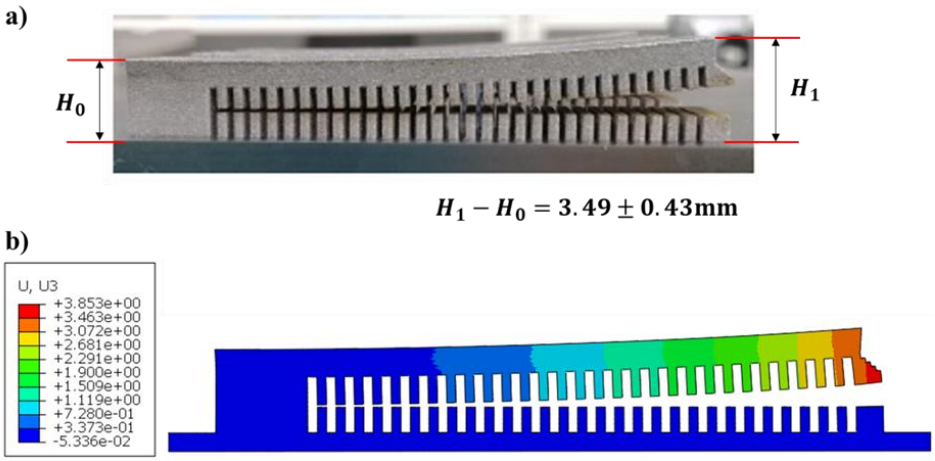

Fig. 14 Distortion of the cantilever after cutting off the support (a) experimental measurement and (b) prediction

Table 6 Multiscale SLM process analysis results

Parameter	Value
Melt pool depth d_m [μm]	131
Melt pool width w_m [μm]	152
Heating time t_h [ms]	0.2
Cantilever distortion [mm]	3.85

In order to investigate the source of residual stress formation, the maximum liquid lifetime (Hu *et al.* 2018) was evaluated at each material point as shown in Fig. 13. A long liquid lifetime of about 0.26 seconds was observed around the top of the support structure whereas a liquid lifetime of about 0.07~0.08 seconds was observed in the surroundings. Although the support was used to aid heat dissipation, the long liquid lifetime in the specific region compared to the rest of the part means that the rate of heat dissipation was uneven and considerably slow during the process. Since the non-uniform heat dissipation is the cause of the residual stress and the part distortion (Gan and Wong 2016), this result provides the insight for the design of the support and the improvement of the part quality. It is also worth noting that since the analysis at the macroscale was conducted with the equivalent body heat flux in this study, the obtained liquid lifetime is not directly in the real time scale considering the scanning paths. However, the contour still can show the relative tendency of the heat dissipation in the part. For future work, the optimal design method of the support to aid heat dissipation with the liquid lifetime contour is suggested.

3.5 Distortion and experimental validation

For validation of the macroscale analysis result, 6 cantilever beams were fabricated and the part distortions were measured after cutting the support with wire electrical discharging machine (EDM) and averaged as shown in Fig. 14(a). The average distortion at the tip of the cantilever in the build direction (Z) was 3.49 mm with a standard deviation of 0.43 mm. The predicted

deformation of the cantilever is also shown in Fig. 14(b). The same bending directions were observed in both the experiment and the simulation. The concave distortion of the cantilever was caused by the release of the tensile stress in the upper region of the printed part after cutting off the support. The predicted distortion was about 3.85 mm which is within the error range. There might be many sources of error since the SLM process involves the setting of several process parameters and the actual laser scanning paths for the whole part were not modeled due to the computational capacity. In particular, a possible key reason for the inaccuracy is the simplification of the multi-layer process into the summation of the mesoscale layers. Due to the fact that the actual process involves hundreds or thousands of layers, the number of mesoscale hatch layers needs to be increased to improve the accuracy of the prediction (Li *et al.* 2017). The computation time for the thermomechanical simulation at macroscale approximately was around 8h on a desktop computer with an Intel core i7-9700 CPU.

The analysis results using the proposed simulation framework are as shown in Table 6. Since the analysis results were based on the multi-scale approach, it can also be said that the results have gained credibility with the evaluation of the process in multiple scales. In the melt pool analysis, the melt pool morphology was investigated as well as the possibility of a defect (lack-of-fusion or keyhole porosity) occurring. If any serious defect was observed in this scale, the error at macroscale could be explained since the thermal and the structural analysis were conducted assuming the continuum material without severe discontinuity. The heating and re-melting cycles predicted with the mesoscale equivalent heat flux also provided insight for the source of the residual stress and the part distortion with the temperature history(e.g liquid lifetime). In other words, the multi-scale SLM process analysis with the proposed melt pool analysis can be a means of process evaluation from the melt pool scale to the part level.

4. Conclusions

In this work, a temperature thread multiscale framework for the SLM process of Ti-6Al-4V with an enhanced melt pool analysis model is proposed to investigate the process from microscale to macroscale. In the microscale melt pool analysis, the melt pool morphology was investigated to evaluate the laser beam process parameters for the formation of a stable melt pool without severe lack-of-fusion and keyhole defects. It was found that the parameters recommended by EOS for the SLM process of Ti-6Al-4V yield a melt pool with sufficient depth and width. The obtained temperature history in the microscale was then used to build a mesoscale equivalent body heat flux model to predict the residual stress and the part distortions at the macroscale. In order to validate the model, an SLM process for fabrication of cantilever was simulated and the result was validated by the experimental measurement of the cantilever distortion. To investigate the source of the inhomogenous thermal distribution, a liquid lifetime contour was investigated. The long liquid lifetime concentrated in the vicinity of the support was observed which means the uneven heat dissipation. For future work, a wider range of process parameters will be investigated for the derivation of the optimal process window based on the multiscale approach.

Acknowledgments

This work was supported by the Korea Evaluation Institute of Industrial Technology (KEIT) grant funded by the Korea government (MOTIE) (No.20004662, Industrial Technology Innovation

Program) and Institute of Engineering Research at Seoul National University. The authors are grateful for their supports.

References

Abaqus, V. (2014), 6.14 Documentation, Dassault Systemes Simulia Corporation, **651**, 6.2.

Ansari, M.J., Nguyen, D.S. and Park, H.S. (2019), "Investigation of SLM process in terms of temperature distribution and melting pool size: Modeling and experimental approaches", *Materials*, **12**(8), 1272. https://doi.org/10.3390/ma12081272.

Boivineau, M., Cagran, C., Doytier, D., Eyraud, V., Nadal, M.H., Wilthan, B. and Pottlacher, G. (2006), "Thermophysical properties of solid and liquid Ti-6Al-4V (TA6V) alloy", *Int. J. Thermophys.*, **27**(2), 507-529. https://doi.org/10.1007/PL00021868.

Boyer, R.R. (1996), "An overview on the use of titanium in the aerospace industry", *Mater. Sci. Eng. A*, **213**(1-2), 103-114. https://doi.org/10.1016/0921-5093(96)10233-1.

Bruna-Rosso, C., Demir, A.G. and Previtali, B. (2018), "Selective laser melting finite element modeling: Validation with high-speed imaging and lack of fusion defects prediction", *Mater. Des.*, **156**, 143-153. https://doi.org/10.1016/j.matdes.2018.06.037.

Buchbinder, D., Meiners, W., Pirch, N., Wissenbach, K. and Schrage, J. (2014), "Investigation on reducing distortion by preheating during manufacture of aluminum components using selective laser melting", *J. Laser Appl.*, **26**(1), 012004. https://doi.org/10.2351/1.4828755.

Çam, G. and Koçak, M. (1998), "Progress in joining of advanced materials", *Int. Mater. Rev.*, **43**(1), 1-44. https://doi.org/10.1179/imr.1998.43.1.1.

Chen, C., Yin, J., Zhu, H., Xiao, Z., Zhang, L. and Zeng, X. (2019b), "Effect of overlap rate and pattern on residual stress in selective laser melting", *Int. J. Mach. Tool. Manu.*, **145**, 103433. https://doi.org/10.1016/j.ijmachtools.2019.103433.

Chen, Q., Liang, X., Hayduke, D., Liu, J., Cheng, L., Oskin, J., Whitmore, R. and To, A.C. (2019a), "An inherent strain based multiscale modeling framework for simulating part-scale residual deformation for direct metal laser sintering", *Additive Manuf.*, **28**, 406-418. https://doi.org/10.1016/j.addma.2019.05.021.

Ciurana, J., Hernandez, L. and Delgado, J. (2013), "Energy density analysis on single tracks formed by selective laser melting with CoCrMo powder material", *Int. J. Adv. Manuf. Tech.*, **68**(5-8), 1103-1110. https://doi.org/10.1007/s00170-013-4902-4.

Das, M., Balla, V. K., Basu, D., Bose, S. and Bandyopadhyay, A. (2010), "Laser processing of SiC-particle-reinforced coating on titanium", *Scripta Materialia*, **63**(4), 438-441. https://doi.org/10.1016/j.scriptamat.2010.04.044.

Dausinger, F. and Shen, J. (1993), "Energy coupling efficiency in laser surface treatment", *ISIJ Int.*, **33**(9), 925-933. https://doi.org/10.2355/isijinternational.33.925.

Del Bello, U., Rivela, C., Cantello, M. and Penasa, M. (1991), "Energy balance in high-power CO_2 laser welding", *Proceedings of the Industrial and Scientific Uses of High-Power Lasers*, Hague, The Netherlands, March.

Dilip, J.J.S., Zhang, S., Teng, C., Zeng, K., Robinson, C., Pal, D. and Stucker, B. (2017), "Influence of processing parameters on the evolution of melt pool, porosity, and microstructures in Ti-6Al-4V alloy parts fabricated by selective laser melting", *Prog. Addit. Manuf.*, **2**(3), 157-167. https://doi.org/10.1007/s40964-017-0030-2.

Fabbro, R. (2010), "Melt pool and keyhole behaviour analysis for deep penetration laser welding", *J. Phys. D Appl. Phys.*, **43**(44), 445501. https://doi.org/10.1088/0022-3727/43/44/445501.

Fan, Z. and Liou, F. (2012), *Numerical Modeling of the Additive Manufacturing (AM) Processes of Titanium Alloy*, in *Titanium Alloys-Towards Achieving Enhanced Properties for Diversified Applications*, 3-28.

Fu, C.H. and Guo, Y.B. (2014), "Three-dimensional temperature gradient mechanism in selective laser melting of Ti-6Al-4V", *J. Manuf. Sci. Eng.*, **136**(6), 061004. https://doi.org/10.1115/1.4028539.

Fukuhara, M. and Sanpei, A. (1993), "Elastic moduli and internal frictions of Inconel 718 and Ti-6Al-4V as a function of temperature", *J. Mater. Sci. Lett.*, **12**(14), 1122-1124. https://doi.org/10.1007/BF00420541.

Gan, M.X. and Wong, C.H. (2016), "Practical support structures for selective laser melting", *J. Mater. Process. Tech.*, **238**, 474-484. https://doi.org/10.1016/j.jmatprotec.2016.08.006.

Gu, D.D., Meiners, W., Wissenbach, K. and Poprawe, R. (2012), "Laser additive manufacturing of metallic components: Materials, processes and mechanisms", *Int. Mater. Rev.*, **57**(3), 133-164. https://doi.org/10.1179/1743280411Y.0000000014.

Gu, D., Wang, H. and Zhang, G. (2014), "Selective laser melting additive manufacturing of Ti-based nanocomposites: The role of nanopowder", *Metall. Mater. Trans. A*, **45**(1), 464-476. https://doi.org/10.1007/s11661-013-1968-4.

Han, Q., Geng, Y., Setchi, R., Lacan, F., Gu, D. and Evans, S.L. (2017), "Macro and nanoscale wear behaviour of Al-Al2O3 nanocomposites fabricated by selective laser melting", *Compos. Part B Eng.*, **127**, 26-35. https://doi.org/10.1016/j.compositesb.2017.06.026.

Herzog, D., Seyda, V., Wycisk, E. and Emmelmann, C. (2016), "Additive manufacturing of metals", *Acta Materialia*, **117**, 371-392. https://doi.org/10.1016/j.actamat.2016.07.019.

Hu, Z., Zhu, H., Zhang, C., Zhang, H., Qi, T. and Zeng, X. (2018), "Contact angle evolution during selective laser melting", *Mater. Des.*, **139**, 304-313. https://doi.org/10.1016/j.matdes.2017.11.002.

Hussein, A., Hao, L., Yan, C. and Everson, R. (2013), "Finite element simulation of the temperature and stress fields in single layers built without-support in selective laser melting", *Mater. Des. (1980-2015)*, **52**, 638-647. https://doi.org/10.1016/j.matdes.2013.05.070.

Kaci, D. A., Madani, K., Mokhtari, M., Feaugas, X. and Touzain, S. (2017), "Impact of composite patch on the J-integral in adhesive layer for repaired aluminum plate", *Adv. Aircraft Spacecraft Sci.*, **4**(6), 679-699. http://doi.org/10.12989/aas.2017.4.6.679.

Kamara, A. M., Wang, W., Marimuthu, S. and Li, L. (2011), "Modelling of the melt pool geometry in the laser deposition of nickel alloys using the anisotropic enhanced thermal conductivity approach", *Proc. Inst. Mech. Eng. Part B J. Eng. Manuf.*, **225**(1), 87-99. https://doi.org/10.1177%2F09544054JEM2129.

Kruth, J. P., Froyen, L., Van Vaerenbergh, J., Mercelis, P., Rombouts, M. and Lauwers, B. (2004), "Selective laser melting of iron-based powder", *J. Mater. Process. Tech.*, **149**(1-3), 616-622. https://doi.org/10.1016/j.jmatprotec.2003.11.051.

Lampa, C., Kaplan, A.F., Powell, J. and Magnusson, C. (1997), "An analytical thermodynamic model of laser welding", *J. Phys. D Appl. Phys.*, **30**(9), 1293. https://doi.org/10.1088/0022-3727/30/9/004.

Lee, K.H. and Yun, G.J. (2020a), "A novel heat source model for analysis of melt pool evolution in selective laser melting process", *Additive Manuf.*, **36**, 101497. https://doi.org/10.1016/j.addma.2020.101497.

Lee, K.H. and Yun, G.J. (2020b), "Prediction of melt pool dimension and residual stress evolution with thermodynamically-consistent phase field and consolidation models during re-melting process of SLM", *Comput. Mater. Continua*, **66**(1), 87-112. http://doi.org/10.32604/cmc.2020.012688.

Leung, C.L.A., Marussi, S., Atwood, R.C., Towrie, M., Withers, P.J. and Lee, P.D. (2018), "In situ X-ray imaging of defect and molten pool dynamics in laser additive manufacturing", *Nature Commun.*, **9**(1), 1-9. https://doi.org/10.1038/s41467-018-03734-7.

Li, C., Liu, J.F., Fang, X.Y. and Guo, Y.B. (2017), "Efficient predictive model of part distortion and residual stress in selective laser melting", *Additive Manuf.*, **17**, 157-168. https://doi.org/10.1016/j.addma.2017.08.014.

Liang, X., Cheng, L., Chen, Q., Yang, Q. and To, A.C. (2018), "A modified method for estimating inherent strains from detailed process simulation for fast residual distortion prediction of single-walled structures fabricated by directed energy deposition", *Additive Manuf.*, **23**, 471-486. https://doi.org/10.1016/j.addma.2018.08.029.

Liu, S., Zhu, H., Peng, G., Yin, J. and Zeng, X. (2018), "Microstructure prediction of selective laser melting AlSi10Mg using finite element analysis", *Mater. Des.*, **142**, 319-328. https://doi.org/10.1016/j.matdes.2018.01.022.

Mercelis, P. and Kruth, J.P. (2006), "Residual stresses in selective laser sintering and selective laser melting", *Rapid Prototyping J.*, **12**(5), 254-265. https://doi.org/10.1108/13552540610707013.

Mills, K.C. (2002), *Recommended Values of Thermophysical Properties for Selected Commercial Alloys*, Woodhead Publishing.

Queva, A., Guillemot, G., Moriconi, C., Metton, C. and Bellet, M. (2020), "Numerical study of the impact of vaporisation on melt pool dynamics in Laser Powder Bed Fusion-Application to IN718 and Ti-6Al-4V", *Additive Manuf.*, **35**, 101249. https://doi.org/10.1016/j.addma.2020.101249.

Rangaswamy, P., Prime, M.B., Daymond, M., Bourke, M.A.M., Clausen, B., Choo, H. and Jayaraman, N. (1999), "Comparison of residual strains measured by X-ray and neutron diffraction in a titanium (Ti–6Al–4V) matrix composite", *Mater. Sci. Eng. A*, **259**(2), 209-219. https://doi.org/10.1016/S0921-5093(98)00893-4.

Roberts, I.A. (2012), "Investigation of residual stresses in the laser melting of metal powders in additive layer manufacturing", Ph.D. Dissertation, University of Wolverhampton, Wolverhampton, England, U.K.

Roy, S., Juha, M., Shephard, M.S. and Maniatty, A.M. (2018), "Heat transfer model and finite element formulation for simulation of selective laser melting", *Comput. Mech.*, **62**(3), 273-284. https://doi.org/10.1007/s00466-017-1496-y.

Seifter, A., Pottlacher, G., Jäger, H., Groboth, G. and Kaschnitz, E. (1998), "Measurements of thermophysical properties of solid and liquid Fe-Ni alloys", *Berichte der Bunsengesellschaft für physikalische Chemie*, **102**(9), 1266-1271. https://doi.org/10.1002/bbpc.19981020934.

Shi, W., Liu, Y., Shi, X., Hou, Y., Wang, P. and Song, G. (2018), "Beam diameter dependence of performance in thick-layer and high-power selective laser melting of Ti-6Al-4V", *Materials*, **11**(7), 1237. https://doi.org/10.3390/ma11071237.

Shrestha, S., Starr, T. and Chou, K. (2019), "A study of keyhole porosity in selective laser melting: single-track scanning with micro-CT analysis", *J. Manuf. Sci. E.*, **141**(7). https://doi.org/10.1115/1.4043622.

Singh, P., Pungotra, H. and Kalsi, N.S. (2017), "On the characteristics of titanium alloys for the aircraft applications", *Mater. Today Proc.*, **4**(8), 8971-8982. https://doi.org/10.1016/j.matpr.2017.07.249.

Trapp, J., Rubenchik, A.M., Guss, G. and Matthews, M.J. (2017), "In situ absorptivity measurements of metallic powders during laser powder-bed fusion additive manufacturing", *Appl. Mater. Today*, **9**, 341-349. https://doi.org/10.1016/j.apmt.2017.08.006.

Vanderhasten, M., Rabet, L. and Verlinden, B. (2008), "Ti–6Al–4V: Deformation map and modelisation of tensile behaviour", *Mater. Des.*, **29**(6), 1090-1098. https://doi.org/10.1016/j.matdes.2007.06.005.

Vastola, G., Zhang, G., Pei, Q.X. and Zhang, Y.W. (2016), "Controlling of residual stress in additive manufacturing of Ti6Al4V by finite element modeling", *Additive Manuf.*, **12**, 231-239. https://doi.org/10.1016/j.addma.2016.05.010.

Verhaeghe, F., Craeghs, T., Heulens, J. and Pandelaers, L. (2009), "A pragmatic model for selective laser melting with evaporation", *Acta Materialia*, **57**(20), 6006-6012. https://doi.org/10.1016/j.actamat.2009.08.027.

Wang, S.L., Sekerka, R.F., Wheeler, A.A., Murray, B.T., Coriell, S.R., Braun, R. and McFadden, G. B. (1993), "Thermodynamically-consistent phase-field models for solidification", *Physica D Nonlin. Phenom.*, **69**(1-2), 189-200. https://doi.org/10.1016/0167-2789(93)90189-8.

Welsch, G., Boyer, R. and Collings, E.W. (1993), *Materials Properties Handbook: Titanium Alloys*, ASM International.

Yadroitsev, I., Gusarov, A., Yadroitsava, I. and Smurov, I. (2010), "Single track formation in selective laser melting of metal powders", *J. Mater. Process. Tech.*, **210**(12), 1624-1631. https://doi.org/10.1016/j.jmatprotec.2010.05.010.

Yap, C.Y., Chua, C.K., Dong, Z.L., Liu, Z.H., Zhang, D.Q., Loh, L.E. and Sing, S.L. (2015), "Review of selective laser melting: Materials and applications", *Appl. Phys. Rev.*, **2**(4), 041101. https://doi.org/10.1063/1.4935926.

Zhang, Z., Huang, Y., Kasinathan, A.R., Shahabad, S.I., Ali, U., Mahmoodkhani, Y. and Toyserkani, E. (2019), "3-Dimensional heat transfer modeling for laser powder-bed fusion additive manufacturing with volumetric heat sources based on varied thermal conductivity and absorptivity", *Opt. Laser Technol.*, **109**, 297-312. https://doi.org/10.1016/j.optlastec.2018.08.012.

Zhao, C., Fezzaa, K., Cunningham, R.W., Wen, H., De Carlo, F., Chen, L., Rollett, A.D. and Sun, T. (2017),

"Real-time monitoring of laser powder bed fusion process using high-speed X-ray imaging and diffraction", *Sci. Reports*, **7**(1), 1-11. https://doi.org/10.1038/s41598-017-03761-2.

EC